Phase-Ramp Reduction in Interseismic Interferograms From Pixel-Offsets

Teng Wang, and Sigurjón Jónsson

Abstract—Interferometric synthetic aperture radar (InSAR) is increasingly used to measure interseismic deformation. Inaccurate satellite–orbit information, expressed as phase ramps across interseismic interferograms, is believed to be one of the main sources of error in such measurements. However, many interferograms exhibit higher phase gradients than expected from the reported orbital accuracy, suggesting that there are other error sources. Here, we show that interferogram phase ramps are in part caused by uncorrected satellite timing-parameter errors. We propose a two-step approach to reduce the phase ramps using pixel-offsets estimated between SAR amplitude images. The first step involves using a digital elevation model (DEM) to estimate absolute timing-parameter errors for the reference image of the SAR dataset and the second step updates the timing parameters of the master image for each interferogram. We demonstrate a clear ramp reduction on interseismic interferograms covering the North Anatolian Fault in eastern Turkey. The resulting interferograms show clear signs of interseismic deformation even before stacking.

Index Terms—Differential interferometric synthetic aperture radar (InSAR), orbital error, phase ramp, pixel-offset.

I. INTRODUCTION

MEASUREMENTS of interseismic deformation near plate boundaries can be used to derive important information for earthquake hazard assessments, such as fault locking depth and slip rate [1], [2]. Unlike the deformation caused by earthquakes and volcanic eruptions, interseismic deformation has a large spatial scale (tens of kilometers) and a low rate of change (tens of millimeters or less per year). These deformation characteristics pose a challenge to geodetic techniques, such as interferometric synthetic aperture radar (InSAR) imaging, for detecting and quantifying interseismic strain accumulation. Several papers have focused on fault locking-depth and slip-rate estimation from interseismic InSAR measurements, e.g., across the North Anatolian Fault (NAF) in Turkey [3]–[5], the San Andreas Fault in California [6], and major faults in Tibet [7]–[9]. As shown in these studies, single interferograms are rarely useful for detecting and quantifying interseismic deformation rates across transform faults, because the interseismic signal is too weak to be distinguished from residual phase ramps and atmospheric effects. As a consequence, the signal-to-noise ratio of the interseismic deformation rate is typically improved by stacking all available unwrapped interferograms or by using time-series analysis to derive a mean line-of-sight velocity map.

The so-called orbital error, which is represented as a long-wavelength phase ramp in interferograms, is one of the main sources of error in interseismic studies using InSAR. Fig. 1 shows two typical examples of interseismic interferograms across the NAF, which exhibit such phase ramps. They were selected from a number of interferograms we formed from 29 SAR images acquired by the Envisat satellite (track 35). All the images were processed using the GAMMA software [10]. We coregistered and resampled all the images onto the grid of a dataset-reference image and formed 104 small baseline interferograms (Fig. 2). We used the 90-m resolution digital elevation model from the Shuttle Radar Topography Mission (SRTM DEM) [11] and DORIS orbital information to remove the topographic phase and filtered the resulting differential interferograms with a two-dimensional (2-D) complex convolution filter [12]. Since the spatial characteristics of phase ramps can be similar to interseismic deformation signals, it is important to eliminate such ramps before using the interferograms in time-series analysis and in estimating interseismic fault model parameters.

In most interseismic studies based on InSAR data, phase ramps have been eliminated from unwrapped interferograms by first fitting a polynomial surface and then removing it from the unwrapped phase [3], [5], [6]. Recently, more sophisticated methods to estimate phase ramps have been reported, e.g., based on wavelet-based regression [13] or based on solving for ramps using a network of time-series SAR images [14]. Although these phase-based methods are easy to implement, their drawbacks are obvious: the phase ramp has to be estimated from an interferogram that is a superimposition of the interseismic deformation signal, orbital errors, atmospheric variations, and other errors. Removal of ramp is therefore likely to be unreliable due to spatial similarities of different phase components, unless external data exist, such as continuous GPS measurements. As a consequence, phase-based ramp removal techniques may distort the interseismic signal and lead to biased modeling results.

Inaccurate satellite orbital information is usually believed to be the main cause of observed phase ramps [13], [14]. The reported orbital errors for ESA radar satellites are several centimeters [15], which would translate to one or two ramp fringes across C-band interferograms ($100 \text{ km} \times 100 \text{ km}$) when projected to the line-of-sight direction. However, over half of the usable interferograms, we formed across the NAF exhibit more than one or two ramp fringes (Fig. 1), suggesting that there are other sources of error. In this paper, we show that phase ramps are
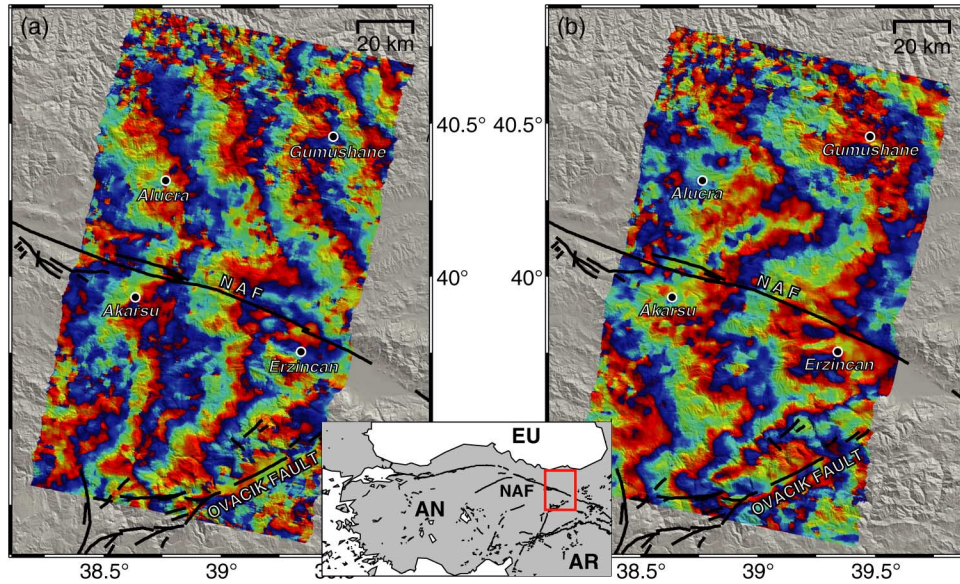
Fig. 1. Phase ramps in two interseismic Envisat interferograms of the NAF in northeastern Turkey. The interferograms span (a) 11 November 2004–11 September 2008 and (b) 12 October 2006–1 October 2009. The inset shows the location of the study area at the boundary between the Eurasian (EU), Anatolian (AN), and Arabian (AR) plates.
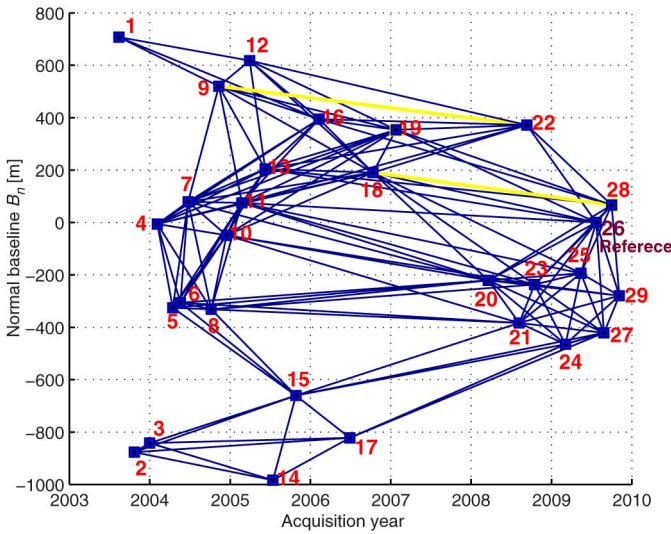

Fig. 2. The interferometric configuration of Envisat descending track 35. B_n is the normal baseline with respect to the dataset reference image. Each square represents an image in the spatial–temporal baseline plane. We connect images with $B_n < 500$ m and acquisition separation less than 5 years to form interferograms that are represented as blue lines. The two interferograms shown in Fig. 1 are represented as yellow lines.

in part caused by uncorrected satellite timing-parameter errors, e.g., local oscillator frequency decay [16]. We then propose, instead of phase-based techniques, a two-step approach to reduce phase ramps using pixel-offsets derived from cross-correlations between amplitude images. We implement the proposed approach in our own InSAR processing software and compare the results with the interferograms derived from standard processing using the GAMMA software package [10] (Fig. 1).

This paper is organized as follows. In Section II, we review the timing-parameter errors and their relations with baseline and incidence angle errors. We then focus on estimating absolute timing errors in Section III, using an external DEM and an

amplitude map averaged from coregistered SAR images. In Section IV, we present the processing steps for estimating the timing-parameter errors for each image in a dataset and in Section V, we offer experimental results from the NAF test site.

II. TIMING-PARAMETER ERRORS IN SAR INTERFEROMETRY

Forming differential interferograms from co-registered SAR images consists of two steps: 1) calculation of the phase difference between master and slave SAR images and 2) subtraction of terrain phases (flat-earth and topographic phases) [17]. In the first step, the phase difference between the SAR images is calculated directly, wheras in the second step the terrain phases are derived from orbital parameters and a DEM. As terrain phases may contain errors, the phase removal in the second step may not be entirely successful, leaving phase ramps in the resulting differential interferograms.

SAR images are acquired in time-range coordinates in which the azimuth line i represents satellite-imaging time and the range pixel j reflects the slant range distance between the satellite and the target. Given a target pixel at location $\vec{P}$ in an interferogram (Fig. 3), the raw phase difference $\phi_{\text{raw}}^{i,j}$ is calculated in the master line-sample (i, j) coordinates, while the terrain phase $\phi_{\text{terrain}}^{t_{\text{az}},\rho}$ for that pixel is calculated from the satellite position information $\vec{S_1}$ and $\vec{S_2}$ and location $\vec{P}$ in the time-range (t_{az}, ρ) coordinates [17]

$$\phi_{\text{terrain}}^{t_{\text{az}},\rho} \approx -\frac{4\pi}{\lambda}\left[B\sin(\theta-\alpha) + \frac{B\cos(\theta-\alpha)}{\rho_1 \sin\theta}h\right] \quad (1)$$

where λ is the radar wavelength, B is the baseline length, where $B = |\vec{S_2} - \vec{S_1}|$ and h is the elevation of the target above a reference ellipsoid. Inaccurate orbital information $\vec{S_1}$ and $\vec{S_2}$ will directly lead to a baseline error and then a phase ramp in a differential interferogram. In addition, the raw phase $\phi_{\text{raw}}^{i,j}$ and the terrain phase $\phi_{\text{terrain}}^{t_{\text{az}},\rho}$ are assumed to be calculated on the same
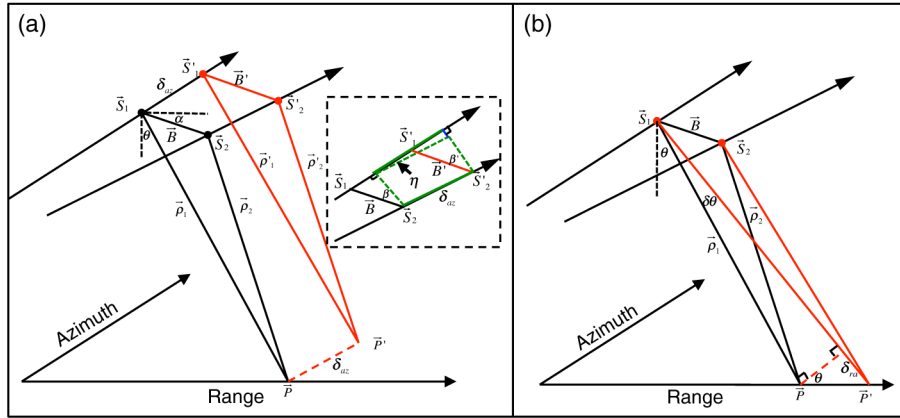
Fig. 3. Interferometric SAR imaging geometry. $\vec{S}_1$ and $\vec{S}_2$ are master and slave antennae positions when ground target $\vec{P}$ is imaged. $\vec{B}$ is baseline, $\vec{\rho}_1$ and $\vec{\rho}_2$ are line-of-sight vectors from the two imaging antennae, θ is the look angle of $\vec{S}_1$, and α is the baseline orientation angle with respect to the horizontal direction. The red lines indicate (a) the along-track error δ_{az} and (b) the radial error δ_{ra} leading to baseline and look angle errors.

ground target $\vec{P}$ imaged at $t_{az}^{i,j}$. However, this assumption is generally not exactly correct due to inaccuracies in mapping an image pixel to the corresponding ground target $\vec{P}$. When we project a pixel onto a reference earth ellipsoid, we first obtain the satellite-imaging position $\vec{S}_1$ and the satellite-target distance ρ. Then, we search for the intersection among a sphere centered at $\vec{S}_1$ with radius ρ, the zero-Doppler plane of the satellite trajectory and the reference ellipsoid [18].

The coordinate systems (i, j) and (t_{az}, ρ) are connected through simple linear relations that include the pulse repetition frequency (PRF) and the sampling frequency (SF), which determine the pixel spacing along the azimuth and range directions, respectively. These linear relations are [18]

$$t_{az} = t_0 + \frac{1}{\text{PRF}} i \tag{2}$$

$$\rho = c\tau_0 + c\frac{1}{\text{SF}} j \tag{3}$$

where t_0 is the acquisition time of the first line, τ_0 is the one-way traveling time of the first pixel, and c is the speed of light. As orbital data for a SAR image typically consist of a certain number of satellite positions at given times, we fit a polynomial to these positions for acquiring the satellite position $\vec{S}_1$ at t_{az}. Even if the satellite position is perfectly described by the polynomial trajectory, i.e., there are no orbital errors, "timing-parameter errors" in (2) and (3) would cause along-track and radial geocoding errors in determining the location of $\vec{P}$ and consequently introduce errors in the terrain phase, $\phi_{\text{terrain}}^{t_{az}, \rho}$.

In the case of an along-track error δ_{az}, the terrain phase would be calculated on target $\vec{P}'$ instead of $\vec{P}$ [Fig. 3(a)] and the corresponding baseline geometry would be changed. If we assume that the two orbital trajectories are coplanar within the length of δ_{az}, then $\delta_{az} \sin \eta = B' \cos \beta' - B \cos \beta$ [Fig. 3(a), inset]. Given the small divergence angle η, we assume that $\beta \approx \beta'$ to derive the corresponding baseline error as

$$\delta B \approx \frac{\delta_{az} \sin \eta}{\cos \beta}. \tag{4}$$

When the range error is δ_{ra}, we can assume that $\rho_1 \delta\theta \approx \frac{\delta_{ra}}{\tan\theta}$ because the length of slant range ρ_1 is much larger than $\frac{\delta_{ra}}{\tan\theta}$ [Fig. 3(b), the red dashed line]. The error $\delta\theta$ in the look angle θ, can then be expressed as

$$\delta\theta \approx \frac{\delta_{ra}}{\rho_1 \tan\theta}. \tag{5}$$

We therefore observe that interferogram phase ramps are caused by two error sources: 1) errors in orbital positions and the polynomial trajectory residues (orbital errors) and 2) timing-parameter errors appearing in the transformation from (i, j) to (t_{az}, ρ) coordinates. It is worth noting that orbital errors and timing-parameter errors cause line-of-sight range changes in different ways. Orbital errors cause phase errors that scale with factor $\frac{\lambda}{4\pi}$ [see (1)]. Timing-parameter errors δ_{az} and δ_{ra} are much larger (meters) than the apparent range-change these errors cause in interferograms (several centimeters or fringes across the whole scene), as the divergence angle η in (4) is small and range ρ_1 in (5) is large. This fact allows us to estimate δ_{az} and δ_{ra} from the pixel-offsets derived from amplitude cross-correlations before the interferogram is formed.

III. ESTIMATION OF ABSOLUTE TIMING-PARAMETER ERRORS FOR THE DATASET REFERENCE IMAGE

With a ground target P with a known position vector $\vec{P}(x, y, z)$ in earth-centered Cartesian coordinates (e.g., from a DEM), we can calculate the SAR image coordinates (i_P, j_P) by first solving for the corresponding SAR azimuth time t_{az} and slant range $|\vec{\rho}|$ [18]

$$|\vec{\rho}| = \left| \vec{S}(t_{az}) - \vec{P} \right| = c\tau \tag{6}$$

$$f_D = -\frac{\lambda}{2|\vec{\rho}|} \vec{\rho} \cdot \vec{v}(t_{az}) \tag{7}$$

$$\frac{x^2 + y^2}{R_e^2} + \frac{z^2}{R_p^2} = 1 \tag{8}$$

where in the earth-centered Cartesian coordinates, $\vec{S}$ and $\vec{v}$ are, respectively, the position and velocity vectors of the satellite at time t_{az}, τ is the one-way travel time between the satellite and the target, and f_D is the Doppler frequency. Then, (i_P, j_P) can be deduced from (2) and (3) with the following timing parameters [19]:

$$i_P = \text{PRF}(t_{az} - t_0) \tag{9}$$

$$j_P = \frac{\text{SF}}{c}(|\vec{\rho}| - c\tau_0). \tag{10}$$

This procedure is called radarcoding, as opposed to its inverse procedure, geocoding. However, as the satellite parameters are not entirely accurate, the image coordinates (i_P, j_P) derived from radarcoding are usually different from the corresponding SAR image coordinates (i_I, j_I). Their differences can be used to estimate the absolute timing-parameter errors of a SAR image as follows:

$$\delta_{az} = (i_P - i_I)\frac{|\vec{v}|}{\text{PRF}} \tag{11}$$

$$\delta_{ra} = (j_P - j_I)\frac{c}{\text{SF}} \tag{12}$$

where $|\vec{v}|/\text{PRF}$ and c/SF are the pixel spacing in the azimuth and the range directions, respectively [18].

In standard InSAR software packages, such as ROI_PAC [20], DORIS [21], and GAMMA, a simulated SAR image is generated using a DEM and orbital parameters. Then, the offsets $\Delta_{sim}^{i,j}$ on image coordinates (i, j) between a SAR master image and the simulated SAR image are estimated using amplitude cross-correlation on many match sub-images (image patches). The obtained $\Delta_{sim}^{i,j}$ therefore correspond to the coordinate differences in (11) and (12). When using reasonably accurate DEMs, such as the SRTM DEM [11], very small $\Delta_{sim}^{i,j}$ are expected if the timing parameters are correct [22]. However, in the NAF case and in many other cases, $\Delta_{sim}^{i,j}$ often exceeds several pixels, according to (11) and (12), leading to tens of meters of absolute timing-parameter errors in both along-track and radial directions.

The absolute timing-parameter errors are assumed to be constant shifts in t_0 and τ_0 in InSAR processing packages like DORIS and they are corrected using the amplitude offsets between the simulated SAR image and the corresponding master. Nevertheless, there is evidence for significant fluctuation in internal satellite clocks, e.g., for the ERS-1 satellite and Envisat [16], [23]. In particular, decay in the local oscillator frequency of Envisat has recently been reported [16]. It is, therefore, reasonable to assume that timing-parameter errors change along both the azimuth and range axes, implying that 2-D or higher-order-correction models are more appropriate than a constant shift. On the other hand, the accuracy of the offset estimations between master and simulated SAR images is generally fairly low, due to speckle noise in SAR images and the relatively low resolution of most DEMs. Consequently, the transformation polynomial parameters for resampling the DEM into SAR coordinates are not entirely accurately estimated and will introduce some topographic-dependent phase errors in the resulting differential interferograms.
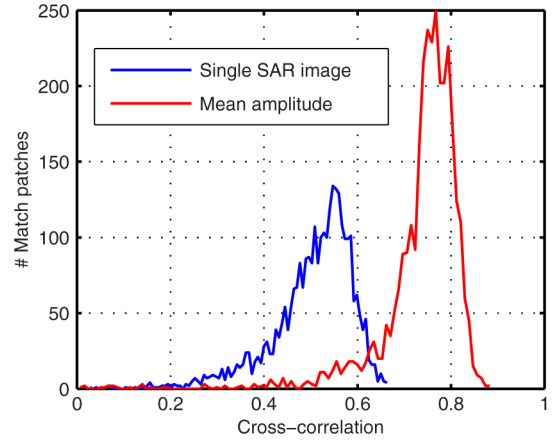

Fig. 4. Cross-correlation histograms between a simulated SAR image, and a single SAR image (blue) and between a simulated SAR image and an incoherent mean amplitude image (red).

Speckle noise in single SAR amplitude images can be significantly reduced by computing the incoherent mean of several coregistered SAR images. For interseismic studies using a multi-image dataset, like the NAF example, we aligned all 29 SAR images with a single master image (we call it the dataset reference image) and computed the mean amplitude map. By using this map, we were able to estimate $\Delta_{sim}^{i,j}$ better than by using the reference SAR image alone. Cross-correlation histograms for 3600 match patches distributed throughout the whole NAF scene showed significantly higher cross-correlation values when using the averaged amplitude map (Fig. 4), implying a clear improvement in the offset estimation.

We estimate the absolute timing-parameter error of the NAF dataset reference image to be about 10 pixels in the azimuth and 3 pixels in the range directions [Figs. 5(a)–(d) and 6 bottom left]. The offsets also exhibit variations along and across the scene that are up to one pixel in size. Therefore, when long multi-frame scenes are processed, the un-compensated errors in the azimuth direction will become large if we simply use a constant shift to correct the timing-parameter errors. It is also interesting to see that the azimuth pixel-offsets changes along the range axis [Fig. 5(b)], which cannot be explained by satellite clock drifts alone. One possible reason is that the radial timing-parameter error δ_{ra} may cause along-track satellite position change, i.e., an azimuth offset, when we project the SRTM DEM into SAR coordinates. As a consequence, the distortion of the simulated SAR image needs to be fitted along the azimuth and the range directions, simultaneously, instead of treating the two directions separately. To deal with the mentioned distortion, we fit a 2-D quadratic polynomial to the pixel-offset field as in conventional SAR-image coregistration (Fig. 6, bottom-left) and align the corresponding DEM with the dataset reference image. One might argue that DEM errors will result in uncertain offset estimates. However, as we are searching for low-frequency changes in the offsets and cross-correlating thousands of match patches, Gaussian-distributed DEM errors [11] will unlikely bias the estimation. In addition, by using the quadratic offset model derived from match-patches with higher correlations, we can better align the DEM with the SAR dataset reference image and therefore reduce the topographic phase in the resulting differential
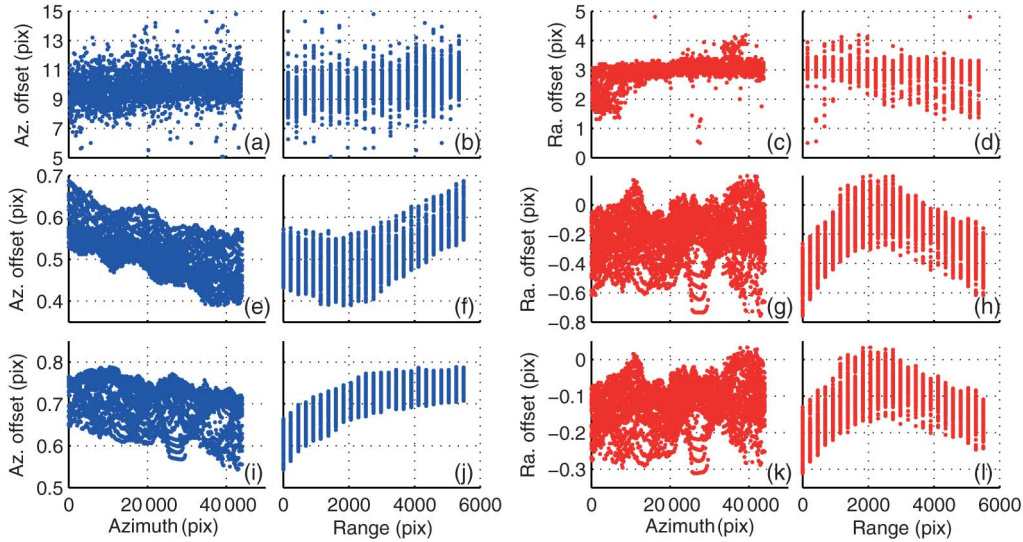
Fig. 5. Timing-parameter errors (in pixels) as a function of azimuth and range, derived from the difference between geometric and amplitude-based pixel-offsets $(\Delta_{\mathrm{geo}}^{i,j} - \Delta_{\mathrm{amp}}^{i,j})$. The first row shows absolute timing errors of the dataset reference image, wheras the second and third rows show relative timing errors (with respect to the reference image) for the two master images of the interferograms shown in Fig. 1. The two left columns (blue) show along-track timing-parameter errors changing along the azimuth and range axes, and the two right columns (red) show the range errors.

interferograms. Alternatively, ground control points can be used to estimate the absolute timing-parameter errors, if we have enough points that can be precisely identified in the amplitude map. This method may be necessary when processing a dataset covering a flat area with no significant topographic features to coregister the SAR images and a DEM.

IV. TIMING-PARAMETER ERROR CORRECTIONS BEFORE INTERFEROGRAM FORMATION

When we use a multi-image InSAR dataset to measure interseismic deformation, we usually start by coregistering all the SAR images onto the grid of a chosen dataset reference image and then construct interferograms from different pairs of coregistered images (interferometric master and slave). Due to similarities in speckle patterns and spatial resolutions between SAR images, the offset estimation between two SAR images should be more accurate than the offsets of the simulated SAR image described in Section III. Thus, based on the estimated absolute timing-parameter errors, we can now estimate relative timing-parameter errors of each image with respect to the dataset reference using pixel-offsets obtained from amplitude cross-correlations.

Differences in imaging geometry result in an offset between a master and a slave SAR image that can be expressed in the master line and sample coordinates as $\Delta^{i,j}$. The pixel-offset can be estimated from orbital information and a DEM [19], [22]. Given the azimuth/range coordinate of the reference image (i^r, j^r), we first calculate the corresponding target position $\vec{P}(x, y, z)$ in the earth-centered Cartesian coordinates. Then, from $\vec{P}(x, y, z)$ and the slave orbital information, we can obtain the corresponding imaging time t_{az}^s and the sensor-target distance $|\vec{\rho}|^s$ of the slave image. Using (9) and (10), we finally calculate the corresponding azimuth/range coordinates (i^s, j^s). The geometrical pixel-offset $\Delta_{\mathrm{geo}}(i, j)$ is then found from the difference between (i^s, j^s) and (i^r, j^r). On the other hand, the amplitude-based offset $\Delta_{\mathrm{amp}}^{i,j}$ is

usually obtained from cross-correlating many image patches and by fitting a 2-D polynomial surface to the resulting offset field. If the timing-related parameter is correct, then $\Delta_{\mathrm{geo}}^{i,j}$ and $\Delta_{\mathrm{amp}}^{i,j}$ should be consistent within a certain error level. However, the actual difference between them shows evident systematic biases (Fig. 5). As the amplitude offsets $\Delta_{\mathrm{amp}}^{i,j}$ are independent from the timing parameters, we can use $\Delta_{\mathrm{geo}}^{i,j} - \Delta_{\mathrm{amp}}^{i,j}$ to estimate the relative along-track and radial timing-parameter errors of the images with respect to the dataset reference image.

On a given number of pixels distributed across the whole scene (here, we use the same pixels as in the absolute timing-parameter error estimation step), we can calculate the geometric offset $\Delta_{\mathrm{geo}}^{i,j}$ using the corrected timing parameters of the dataset reference image and the given DEM in SAR coordinates. The amplitude-based $\Delta_{\mathrm{amp}}^{i,j}$ can, on the other hand, be obtained directly from the polynomial parameters estimated during the initial resampling of the SAR images onto the dataset-reference image grid. The difference between the two offset estimations provides information about the relative timing-parameter errors shown in Figs. 5(e)–(h) and 4(i)–(l). Compared to absolute timing-parameter errors, the relative timing-parameter errors are only a fraction of a pixel, indicating that the main part of the error has been corrected for in the previous steps. Along the range dimension, both the azimuth and range offsets show evident quadratic behavior [Figs. 5(f), (h), (j), and (l) and 6, bottom], suggesting that systematic timing-parameter errors are responsible for the main part of the obtained relative offsets. Moreover, the azimuth timing-parameter errors change along both axes [Figs. 5(e), (f) and 4(i), (j)], demonstrating again that a constant shift or even a linear clock drift model along the azimuth axis cannot correct the timing-parameter errors properly. However, irregular fluctuations can also be observed, especially when we plot the range offsets along azimuth axis [Figs. 5(g) and 4(k)]. Here, the amplitude-based pixel-offsets come from the global image-transformation polynomial that does not account for local topography effects, despite the range pixel-offsets being
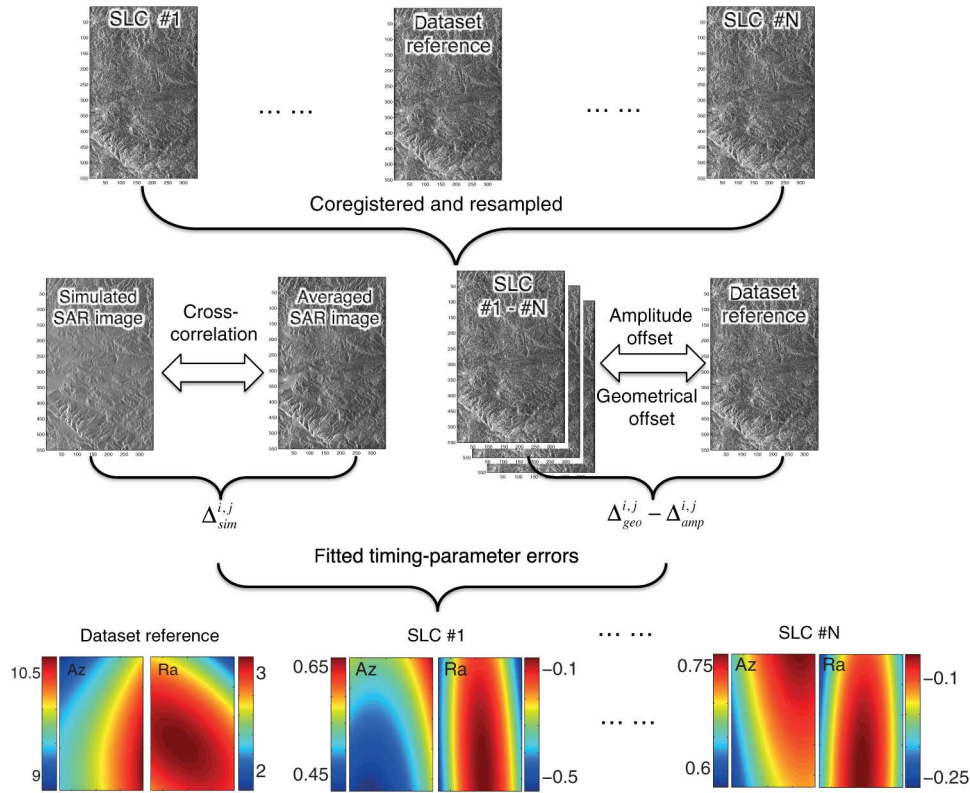
Fig. 6. The workflow of the method proposed here. The six sub-images at the bottom are the 2-D pixel-offset fields that correspond to Fig. 5. The pixel-offset trends of the dataset reference image are fitted from Fig. 5(a)–(d); those below SLC #1 are from Fig. 5(e)–(g); and those below SLC #N are from Fig. 5(h)–(k) and given in pixels.

elevation dependent [22]. The geometric pixel-offset estimation, on the other hand, includes elevation variations from the external DEM. These offset fluctuations [Figs. 5(g) and 4(k)] are, therefore, topography-related pixel-offset residues coming from the difference between the two methods.

Besides satellite clock drift, there is another timing-parameter-error source we have to be concerned about when carrying out multi-image InSAR analysis. After the initial coregistration to the dataset reference image and image resampling, all the images (except for the dataset reference image) are distorted by the transformation polynomial, and therefore their line-sample coordinates do not reflect the true geocoding parameters t_{az} and ρ from (2) and (3). The constant offset can be compensated for, by updating the first azimuth time t_0 and the first slant range ρ_0 after resampling, as is done in standard InSAR software packages. However, higher-order coefficients of the image transformation polynomial exist as well and will still introduce errors in $\vec{S}_1$ and $\vec{\rho}_1$ through incorrect i and j. We should therefore use the original line-sample coordinates of the interferometric master to obtain $\phi_{\text{terrain}}^{i,j}$. This can be achieved by calculating the pixel-offset $\Delta_{\text{amp}}^{i,j}$ from the image transformation polynomial between the dataset reference image and the other images. Then, the original coordinates can be recovered by adding back $\Delta_{\text{amp}}^{i,j}$ before calculating $\phi_{\text{terrain}}^{i,j}$.

It is worth noting that in the timing-parameter error estimation steps, the satellite position errors (orbital errors) in the along-track and radial directions also introduce shifts in δ_{az} and δ_{ra}. However, since orbital errors are in centimeter-level [15], while timing-parameter errors often reach tens of meters, the latter

make up the main part of the obtained pixel-offsets. Recall that orbital errors cause line-of-sight range changes in different ways and, in our method, we only correct the errors (both timing-related and orbital errors) leading to residual phases from (4) and (5), rather than correcting the baseline errors induced directly from inaccurate satellite positions.

In summary, the timing-parameter errors for an InSAR dataset can be corrected as follows (see also Fig. 6). First, the absolute timing-parameter errors are estimated for the dataset-reference image with respect to a simulated SAR image from a DEM, recorded as pixel-offsets $\Delta_{\text{sim}}^{i,j}$. Then, the relative timing-parameter errors between each image and the dataset reference are estimated from the pixel-offset differences between $\Delta_{\text{geo}}^{i,j}$ and $\Delta_{\text{amp}}^{i,j}$. Finally, the high-order distortion from the resampling polynomial is compensated in each SAR image. Since the timing-related errors are estimated on the same image patches and given in pixels, we at last fit a 2-D quadratic polynomial to update the interferometric master coordinates i, j, during the terrain phase calculation step. Note that in our interferogram examples processed by GAMMA (Figs. 1 and 8, top row), the constant part of the timing-parameter errors has already been corrected.

The precision of the estimated timing-parameter errors relies on the pixel-offset estimation. While the offset estimation can be significantly improved by using an averaged amplitude map, the pixel-offset determination between an average amplitude map and a simulated SAR image can be limited by the resolution of the DEM used. For the relative timing-parameter errors, the accuracy depends on the pixel-offset difference between $\Delta_{\text{geo}}^{i,j}$
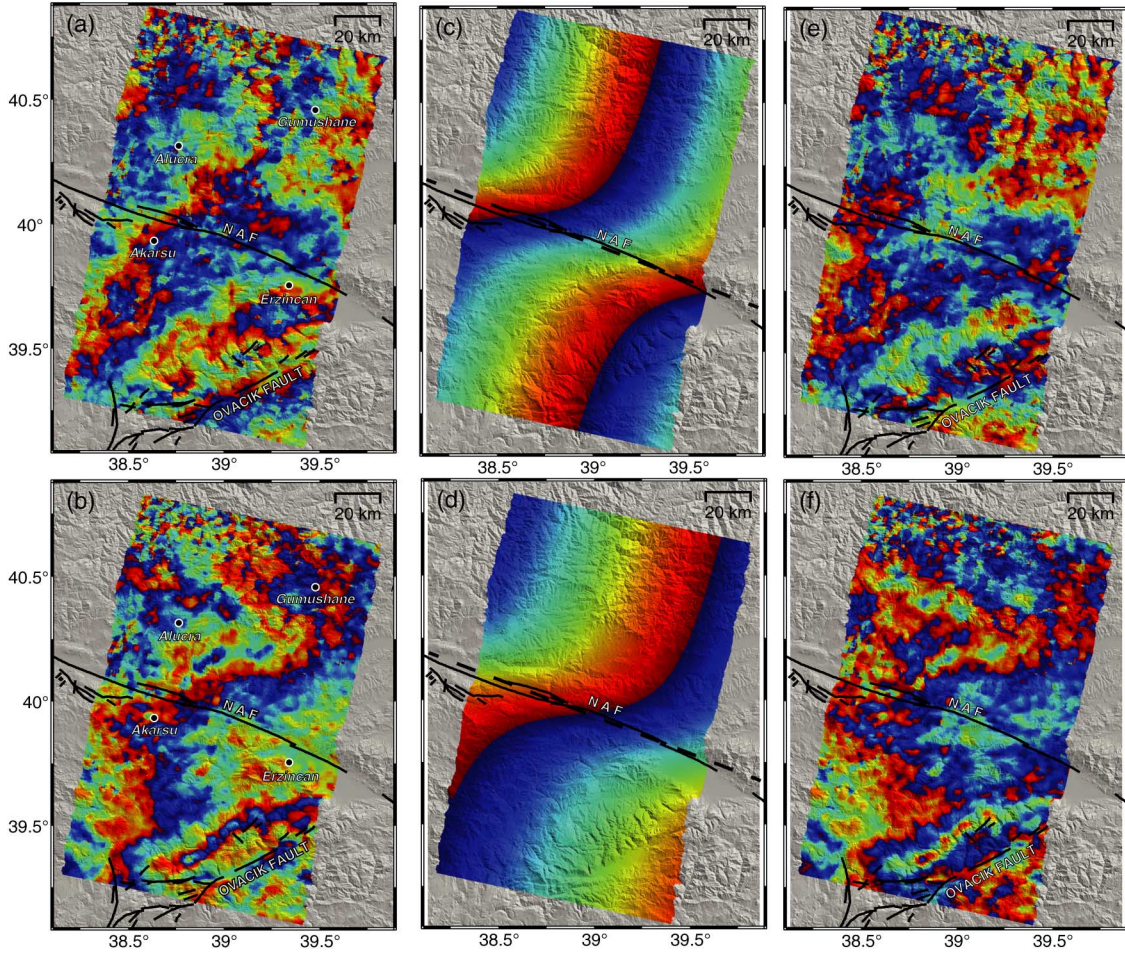
Fig. 7. Interseismic interferograms (same as in Fig. 1) after correcting timing-parameter errors (a), (b) and simulated interferograms (c), (d) containing model-predicted deformation and across-track phase ramps due to orbital errors. The residual phase variations are shown on the right (e), (f) and are mainly due to atmospheric delays and DEM errors.

and $\Delta_{\mathrm{amp}}^{i,j}$. The accuracy of $\Delta_{\mathrm{amp}}^{i,j}$ relies on the image coregistration and should be within 1/8 pixel (about 0.6 m in the azimuth and 1 m in the range directions in Envisat images) for achieving interferometry [17]. The accuracy of $\Delta_{\mathrm{geo}}^{i,j}$, on the other hand, depends on the orbital data and the DEM and should be better than that of $\Delta_{\mathrm{amp}}^{i,j}$, given reasonable baseline information and SRTM DEM [22]. As pointed out by [24], meter-level accuracy can be achieved for the ERS and Envisat systems when using tie-points. This accuracy level should be a reasonable approximation of the achievable precision for correcting the timing-parameter error using pixel-offsets. The pixel-offsets we estimated in this paper (Fig. 5) indicate that the timing-parameter errors are about 50 m in the azimuth and 24 m in the range directions and their variations along and across the scene are up to about 8 m in azimuth and 12 m in range, i.e., about 1.5 pixels in size. While these numbers appear rather unacceptable when compared to the precise InSAR measurements, they are quite typical for ERS and Envisat images.

V. RESULTS AND DISCUSSION

Vegetation and seasonal snow cause significant temporal decorrelation in interferograms of the NAF region, causing only

47 of the 104 interferograms we formed to be coherent. We applied the method described above to all 25 interferograms exhibiting multi-fringe ramps, and 19 of them showed significant phase-ramp reduction. The number of residual ramp fringes was typically reduced from three or four to about one or fewer. This shows that our method, which does not rely on any phase information, provides considerable help to the subsequent phase-based processing steps, such as unwrapping, orbital ramp fitting, removal, etc.

After correcting the timing-parameter errors for the two interferogram examples shown in Fig. 1, we can see approximately one fringe shift from top to bottom in each interferogram (Fig. 7). Considering the wavelength (56 mm) and the incidence angle (23°) of Envisat IS2 data, a single fringe shift means that 28 mm line-of-sight deformation took place across the NAF during the three to four year time-span, showing the expected $\sim 20\ \mathrm{mm/year}$ horizontal motion across the locked fault [25]. We can compare the observed deformation to predictions based on a simple dislocation model. Given an infinitely long vertical strike-slip fault in an elastic half-space, the horizontal fault-parallel motion u across the fault can be described as [26]

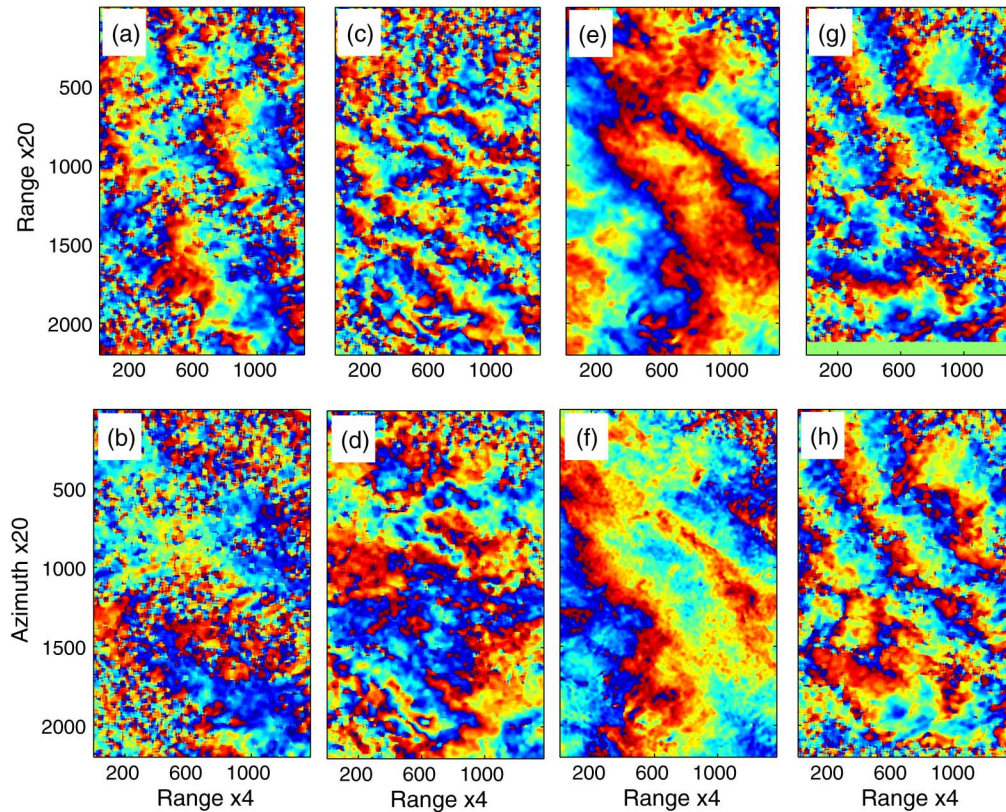$$u = \frac{s}{\pi}\tan^{-1}\left(\frac{x}{d}\right) \qquad (13)$$

Fig. 8. Four interseismic Envisat interferograms of the NAF before (top row) and after (bottom row) applying the proposed timing-parameter correction method. The interferograms span (a) and (b) 14 August 2003–31 March 2005, (c) and (d) 12 October 2006–23 July 2009, (e) and (f) 7 August 2008–27 August 2009, (g) and (h) 20 May 2004–16 October 2008.

where s is the fault-slip velocity below the fault-locking depth d and x is a perpendicular distance from the fault.

Using a locking depth of 19 km and deep slip velocity of 23 mm/year (approximate values from [5]), we calculated the predicted horizontal deformation and projected it into the line-of-sight direction [Fig. 7(c) and (d)]. In addition, we added 1.5 and 1 across-track fringes to the two simulated interferograms, respectively [Fig. 7(c) and (d)], since it is evident that around one residual fringe still remains after the timing-parameter correction, probably caused by inaccurate orbital information [Fig. 7(a) and (b)]. The similarity between the corrected and simulated interferograms demonstrates that the proposed ramp-reduction method preserves the low-frequency deformation signal well. In particular, the interferograms exhibit the expected arc-tangent shape of the interseismic deformation across the NAF in Fig. 7(b), which is usually not visible in individual interferograms before stacking. The residuals after subtracting Fig. 7(c) and (d) from (a) and (b) are fairly flat and mostly exhibit noise [Fig. 7(e)–(f)]. There are localized residual fringes in the southeastern corner of Fig. 7(e)–(f) near the Ovacik Fault that are unlikely caused by deformation because there is no evidence of localized deformation appearing in this region [5], [25]. For the most part, these fringes are likely topography-dependent atmospheric signals, which can be reduced in what would be the next steps of standard time-series InSAR processing or stacking.

To further validate the reliability of our proposed timing-parameter corrections, we present another four interferogram examples taken from the processed interferograms (Fig. 8). Here, the wrapped interferograms are shown in radar coordinates and are somewhat more affected by decorrelation than in the previous two examples. The timing-parameter correction significantly reduces the phase ramps in the first two examples. The improvement is particularly impressive for the example in Fig. 8(c), where multiple fringes are almost completely eliminated. This shows that our method can also be used in cases of low coherence. Interferograms that exhibit small residual ramps before and after the correction [e.g., Fig. 8(e) and (f)] are usually made from image-pairs with short temporal baselines, implying limited satellite clock drift. The ramp fringes remain almost unchanged in the last example [Fig. 8(g) and (h)]. For such interferograms, the residual ramp fringes are probably caused by other phenomena, such as inaccurate orbital information or strong atmospheric gradients.

We unwrapped the interferograms shown in this paper and stacked them to generate two deformation-velocity maps, one made from interferograms formed using standard processing and another from our processor (Fig. 9). We excluded one dataset from the stacks [Fig. 8(g) and (h)] because multiple fringes remained in this case after correcting the timing-parameter errors. The standard deviation of velocities along two profiles that are parallel to and 20 km away from the NAF is reduced from about 7.2 mm/year to 2.6 mm/year after applying the proposed timing-parameter error correction. Interferogram stacking enhances signals that correlate with time, but suppresses other
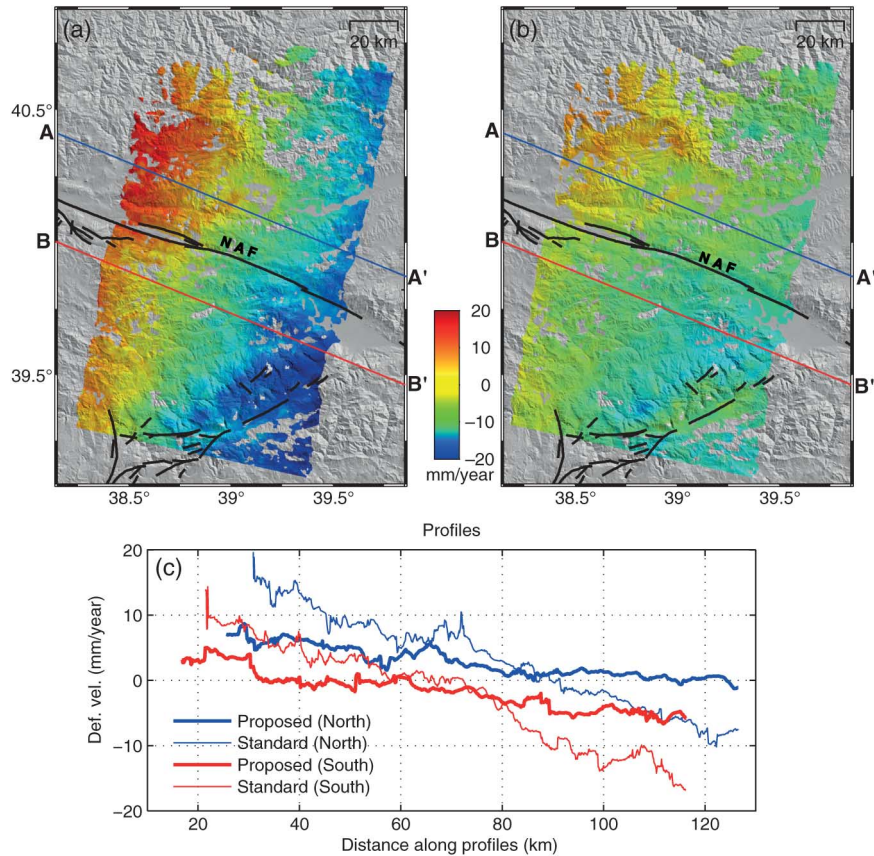
Fig. 9. InSAR velocity maps across the NAF derived from stacking interferograms formed by (a) standard processing and (b) our proposed method. Velocities along two profiles parallel to the NAF, 20 km to the north (A−A′, blue lines) and to the south (B−B′, red lines) are shown in (c). The thin lines are from standard processing, while the thick lines are from our proposed method.

signals. Therefore, the strong trend seen in Fig. 9(a) indicates that the ramp signals are correlated with time. Using ~10 000 Envisat ASAR images from a 10-year period, Marinkovic and Larsen [16] showed recently that the local oscillator frequency of Envisat decayed across time, causing multi-fringe phase ramps across interferograms with significant temporal baselines (years). They proposed a simple exponential decay model to reduce these phase ramps to improve InSAR results. They also pointed out that the oscillator frequency in the ERS did not decay or systematically change across time and therefore could not easily be modeled. Nevertheless, with our proposed method, the timing-parameter error can be corrected for every dataset without a decay or other time-dependent model.

As presented here, timing-parameter corrections should be introduced as a pre-processing step before applying any phase-based ramp-reduction method. In advanced methods that correct orbital errors from residual fringes, e.g., [14], the orbital errors could be better modeled and estimated after first correcting the residual ramp fringes due to the timing-parameter errors, as the initial ramp fringes are caused by a combination of orbital and timing-parameter errors. We have not yet tested our method on data from other SAR sensors, but the proposed method could easily be integrated into standard InSAR processing chains of all kinds of SAR data. For high-resolution missions, the relative timing-parameter errors could be estimated with higher precision, as the pixel-spacing is significantly smaller than in the

Envisat and ERS data. However, identifying several ground control points should be a better option than using DEM-simulated SAR images when estimating the absolute timing-parameter shifts in high-resolution settings.

VI. CONCLUSION

Inaccurate timing parameters are an important source of error in InSAR applications and they are usually corrected using only a constant starting-time shift. Our study shows that timing-parameter variations are often responsible for the main part of observed phase ramps and they are often misinterpreted as resulting from orbital errors in many cases. Here SAR amplitude information plays an important role in keeping the timing-parameter error correction independent of the phase measurement. Our proposed method can be helpful in improving InSAR analysis of many geophysical phenomena such as inter-seismic strain accumulation and post-glacial rebound.

REFERENCES

[1] P. Segall, *Earthquake and Volcano Deformation*, Princeton, NJ, USA: Princeton Univ. Press, 2010.

[2] S. Metzger, S. Jónsson, and H. Geirsson, "Locking depth and slip-rate of the Húsavík Flatey fault, North Iceland, derived from continuous GPS data 2006–2010," *Geophys. J. Int.*, vol. 187, pp. 564–576, 2011.

[3] T. Wright, B. Parsons, and E. Fielding, "Measurement of interseismic strain accumulation across the North Anatolian Fault by satellite radar interferometry," *Geophys. Res. Lett.*, vol. 28, no. 10, pp. 2117–2120, 2001.

[4] M. Motagh, J. Hoffmann, B. Kampes, M. Baes, and J. Zschau, "Strain accumulation across the Gazikoy–Saros segment of the North Anatolian Fault inferred from Persistent Scatterer Interferometry and GPS measurements," *Earth Planet. Sci. Lett.*, vol. 255, no. 3–4, pp. 432–444, 2007.

[5] J. Walters, R. J. Holley, B. Parsons, and T. J. Wright, "Interseismic strain accumulation across the North Anatolian Fault from Envisat InSAR measurements," *Geophys. Res. Lett.*, vol. 38, no. 5, pp. 1–5, 2011.

[6] Y. Fialko, "Interseismic strain accumulation and the earthquake potential on the southern San Andreas fault system," *Nature*, vol. 441, pp. 968–971, 2006.

[7] T. Wright, B. Parsons, P. C. England, and E. J. Fielding, "InSAR observations of low slip rates on the major faults of western Tibet," *Science*, vol. 305, no. 5681, pp. 236–239, 2004.

[8] J. Elliott, J. Biggs, B. Parsons, and T. J. Wright, "InSAR slip rate determination on the Altyn Tagh Fault, northern Tibet, in the presence of topographically correlated atmospheric delays," *Geophys. Res. Lett.*, vol. 35, pp. 1–5, 2008.

[9] O. Cavalie *et al.*, "Measurement of interseismic deformation across the Haiyuan Fault by radar interferometry," *Earth Planet. Sci. Lett.*, vol. 275, pp. 246–257, 2008.

[10] C. Werner, U. Wegmuller, T. Strozzi, and A. Wiesmann, "Gamma SAR and interferometric processing software," in *Proc. ERS-ENVISAT Symp.*, Gothenburg, Sweden, 2000.

[11] G. Farr *et al.*, "The shuttle radar topography mission," *Rev. Geophys.*, vol. 45, RG2004, 2007.

[12] D. Perissin and T. Wang, "Repeat-pass SAR interferometry with partially coherent targets," *IEEE Trans. Geosci. Remote Sens.*, vol. 50, no. 1, pp. 271–280, Jan. 2012.

[13] M. Shirzaei and T. Walter, "Estimating the effect of satellite orbital error using wavelet-based robust regression applied to InSAR deformation data," *IEEE Trans. Geosci. Remote Sens.*, vol. 49, no. 11, pp. 4600–4605, Nov. 2011.

[14] H. Bähr and R. Hanssen, "Reliable estimation of orbit errors in spaceborne SAR interferometry, the network approach," *J. Geodesy*, vol. 86, pp. 1147–1164, 2012.

[15] E. Doornbos and R. Scharroo, "Improved ERS and ENVISAT precise orbit determination," in *Proc. 2004 ENVISAT and ERS Symp.*, Salzburg, Austria, 6–10 Sep. 2004, ESA Conf., vol. SP-572, 2005.

[16] P. Marinkovic and Y. Larsen, "Consequences of long-term ASAR local oscillator frequency decay–an empirical study of 10 years of data," presented at Living Planet Symp., Edinburgh, U.K., 2013.

[17] R. Hanssen, *Radar Interferometry—Data Interpretation and Error Analysis*, Dordrecht, The Netherlands: Kluwer Academic Publishers, 2001.

[18] G. Schreier, *SAR Geocoding: Data and Systems*, Heidelberg, Germany: Wichmann, 1993.

[19] E. Sansosti, P. Berardino, M. Manunta, F. Serafino, and G. Fornaro, "Geometrical SAR image registration," *IEEE Trans. Geosci. Remote Sens.*, vol. 44, no. 10, pp. 2861–2870, Oct. 2006.

[20] A. Rosen, S. Hensley, G. Peltzer, and M. Simons, "Updated repeat orbit interferometry package released," *Eos Trans. AGU*, vol. 85, no. 5, p. 47, 2004.

[21] B. Kampes and S. Usai, "Doris: The delft object-oriented radar interferometric software," in *Proc. ITC 2nd ORS Symp.*, Aug. 1999, pp. 241–244 [CD-ROM].

[22] D. O. Nitti, R. F. Hanssen, A. Refice, F. Bovenga, and R. Nutricato, "Impact of DEM-assisted coregistration on high-resolution SAR interferometry," *IEEE Trans. Geosci. Remote Sens.*, vol. 49, no. 3, pp. 1127–1143, Mar. 2011.

[23] D. Massonnet and H. Vadon, "ERS-1 internal clock drift measured by interferometry," *IEEE Trans. Geosci. Remote Sens.*, vol. 33, no. 2, pp. 401–408, Mar. 1995.

[24] M. Eineder, C. Minet, P. Steigenberger, X. Cong, and T. Fritz, "Imaging geodesy-toward centimeter-level ranging accuracy with terraSAR-X," *IEEE Trans. Geosci. Remote Sens.*, vol. 49, no. 2, pp. 661–671, Feb. 2011.

[25] R. Reilinger *et al.*, "GPS constraints on continental deformation in the Africa-Arabia-Eurasia continental collision zone and implications for the dynamics of plate interactions," *J. Geophys. Res.*, vol. 111, pp. 1–26, 2006.

[26] G. D. Savage and R. O. Burford, "Geodetic determination of relative plate motion in central California," *J. Geophys. Res.*, vol. 5, pp. 832–845, 1973.
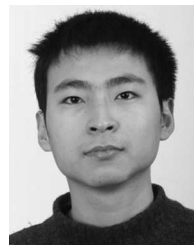
Teng Wang was born in Xinxiang, China, in 1980. He received the B.Eng. and M.Eng. degrees in photogrammetry and remote sensing from Wuhan University, Wuhan, China, in 2003 and 2006, respectively, and the Ph.D. degree in information technology from Wuhan University and the Politecnico di Milano, Milan, Italy, in 2010.

Since October 2010, he works as a Post-Doctoral Researcher at King Abdullah University of Science and Technology (KAUST), Thuwal, Saudi Arabia. His current research interests include InSAR and offset tracking techniques, and their applications in geophysical studies.

Dr. Wang is a Member of the American Geophysical Union. He received the IEEE JSTARS best paper award in 2012.

Sigurjón Jónsson was born in Húsavík, North Iceland, in 1971. He received the B.S. and M.S. degrees in geophysics from the University of Iceland, Reykjavík, Iceland, in 1994 and 1996, respectively, the M.S degree in electrical engineering, and the Ph.D. degree in geophysics from Stanford University, Stanford, CA, USA, in 2002.

From 2004 to 2009, he was a Senior Researcher and Lecturer with the Institute of Geophysics, Swiss Federal Institute of Technology (ETH) Zürich, Zürich, Switzerland. Currently, he holds an Associate Professorship in geophysics at King Abdullah University of Science and Technology (KAUST), Thuwal, Saudi Arabia. His thesis work focused on using InSAR measurements to constrain deformation models of volcanic and seismic processes.

Dr. Jónsson is a Member of the American Geophysical Union and the European Geosciences Union. He was awarded the Reginald A. Daly Postdoctoral Fellowship at the Department of Earth and Planetary Sciences, Harvard University, Cambridge, MA, USA, in 2002, where he continued applying InSAR to the various geophysical problems.